Microstructure and strength modelling of Al–Cu–Mg alloys during non-isothermal treatments
Part 1 – Controlled heating and cooling

I. N. Khan and M. J. Starink*

A model is developed to predict the precipitation kinetics and strengthening in Al–Cu–Mg alloys during non-isothermal treatments consisting of controlled heating and cooling. The prediction of the precipitation kinetics is based on the Kampmann and Wagner model. The precipitation strengthening by the shearable Cu–Mg co-clusters is modelled on the basis of the modulus strengthening mechanism and the strengthening by the non-shearable S phase precipitates is based on the Orowan looping mechanism. The model predictions are verified by comparing with hardness, transmission electron microscopy and differential scanning calorimetry data on 2024-T351 aluminium alloys. The microstructural development and strength predictions of the model are generally in close agreement with the experimental data.

Keywords: Aluminium alloys, Ageing, Modelling, Phase transformations, Co-clusters

Introduction

Non-isothermal processes may involve very rapid temperature changes, such as in welding of aluminium alloys where the heating rate may be as high as several thousand °C s^{-1}.[1–4] Modelling of the reactions occurring in these processes is important for optimising the materials and processes, but as these thermal flow conditions are difficult to reproduce and measure in the laboratory, verification of the models will be difficult. To devise and test a model capable of predicting microstructure evolution and resulting strength during (and subsequent to) these fast, non-isothermal treatments, the authors have divided the modelling of non-isothermal treatments into two parts. In the present work the authors have modelled the strength changes during controlled heating/cooling, which are measured using calorimetry to test/verify the model predictions *in situ* and in a companion paper the model is applied to welding.

The model is developed for Al–Cu–Mg alloys, and is specifically applied to 2×24 alloys which have a composition of about Al–2 at.-%Cu–1·5 at.-%Mg. These alloys are used in commercial aircraft structures such as fuselage and lower wing surface due to their good damage tolerance, resistance to fatigue crack propagation and fracture toughness.[5] In these alloys, high strength is achieved by the precipitation strengthening mechanism.[6,7] In Al–Cu–Mg alloys with Cu/Mg atomic ratio in the order of 1, the interpretation of the precipitation reaction is controversial with regards to the structure and chemistry of some of the (pre-) precipitates appearing during ageing.[8–12] One of the first precipitation sequences proposed in these alloys is[13]

$$\alpha_{ss}\rightarrow\text{GPB zones}\rightarrow\text{GPB2/S}''\text{ phase}\rightarrow\text{S}'\rightarrow\text{S phase}$$

where α_{ss} stands for super saturated solid solution, GPB stands for Guinier–Preston–Bagaryatsky zones, S′ and GPB2/S″ are metastable intermediate phases and S (Al_2CuMg) is the equilibrium phase.

In recent studies, the metastable S′ phase has been accepted as continuous rather than distinct to the equilibrium S phase due to very similar composition and crystal structure.[14–16] The existence of GPB zones has often been cited in the literature but with no confirmed supporting microstructural evidence and recent three-dimensional atomic probe analysis studies indicate the formation of Cu–Mg co-clusters during initial ageing in these alloys.[16] The co-clusters can range in size from just a few atoms (essentially a sub nanometre scale cluster) to hundreds of atoms.[17,18] Although the intermediate phase, alternately termed GPB2 or S″, has been observed in these alloys, it has very limited influence on the hardening in alloys with 1 wt-%Cu or more.[16] In the present work, the authors follow a simplified precipitation reaction,[16] which is also consistent with the two stage strengthening observed in these alloys[19,20]

$$\alpha_{ss}\rightarrow\text{Cu}-\text{Mg coclusters}\rightarrow\text{S phase precipitates}$$

The present work develops a two precipitate ageing model valid for heat treatments covering a 500°C range and the first attempt to test a model based on the

Materials Research Group, School of Engineering Sciences, University of Southampton, Southampton, SO17 1BJ, United Kingdom

*Corresponding author, email m.j.starink@soton.ac.uk

Published by Maney on behalf of the Institute
Received 17 January 2008; accepted 11 April 2008
DOI 10.1179/174328408X317020

Kampmann and Wagner (KW) type numeric model[21–28] against measurements of the heat flow during heat treatment over a range covering 500°C, and the precipitate size and hardness following these treatments. It follows on from earlier work on a model for strengthening in Al–Cu–Mg alloys during isothermal treatments.[29]

Model

The model presented in the present work consists of two integrated components for the prediction of the precipitation kinetics during ageing and evaluation of the strengthening as consequence of the microstructural development.

Precipitation kinetics model

The aim of the microstructural model is to predict the volume fraction of the Cu–Mg co-clusters and the average size and volume fraction of the S phase precipitates. The modelling of precipitation kinetics of the S phase is based on the model generally named after Kampmann and Wagner.[21,25,30–32] The authors will apply the model in pseudo binary form, which will yield good approximations for the alloy considered with Cu/Mg ratio close to 1, and avoid complications inherent in a ternary formulation. In the model, new precipitates forming during each time step are treated as an individual group and their growth (or dissolution) is evaluated in the subsequent time steps as a group.

In the model the fundamental parameters are the semiequilibrium solvi for the Cu–Mg co-clusters and the S phase precipitates, which are determined using the regular solution model (or solution product equation), i.e.[33]

$$\left(c_{\mathrm{e}}^{\mathrm{Cu}}\right)\left(c_{\mathrm{e}}^{\mathrm{Mg}}\right)=k_1\exp\left(\frac{-\Delta H}{RT}\right) \tag{1}$$

where k_1 is a constant and ΔH is the formation enthalpy taken as 38 and 75 kJ mol^{-1} for the co-clusters and the S phase respectively (*see* Ref. 33 similar values are identified in Ref. 17). The 2024 aluminium alloy is assumed to be pseudobinary with the concentrations of copper and magnesium in the matrix remaining equal during the entire ageing process (the Cu/Mg ratio is $\sim$1 for both for the S phase precipitates and the Cu–Mg co-clusters). Thus the semiequilibrium solvus of the solute in the co-clusters and the S phase precipitates is evaluated by

$$c_{\mathrm{e}}=k_2\left[\exp\left(\frac{-\Delta H}{RT}\right)\right]^{0{\cdot}5} \tag{2}$$

where k_2 is a constant, c_{e} is the solvus of the co-clusters ($c_{\mathrm{e}}^{\mathrm{cl}}$) or the S phase precipitates ($c_{\mathrm{e}}^{\mathrm{S}}$). k_1 and k_2 are derived by considering the stability limit of the co-clusters and the S phase precipitates. From differential scanning calorimetry (DSC) data of 2024 Al–Cu–Mg alloys those stability limits are taken as 250 and 490°C respectively.[10,15–17]

The nucleation rate and the critical size of the S phase precipitates are determined on the basis of the classical nucleation theory,[34] which is generally considered valid for the binary alloys and not strictly applicable for multicomponent alloys. In the model, however, this is overcome by assuming the alloy as pseudobinary (nucleation and growth of the precipitates is controlled by the diffusion of copper). The nucleation rate J of the precipitates is calculated in the model by[30,31]

$$J=N_{\mathrm{v}}\frac{k_{\mathrm{b}}T}{h}\exp\left(-\frac{4}{3}\frac{\pi\gamma_{\mathrm{n}}r^{*2}}{RT}+\frac{Q_{\mathrm{d}}}{RT}\right) \tag{3}$$

where γ_{n} is the interfacial energy, Q_{d} is the activation energy for diffusion of the solute in the matrix, k_{b} is the Boltzmann constant, h is the Planck constant, N_{v} is the number of the nucleation sites per unit volume estimated as the number of solute atoms per unit volume.[35] r^* is the critical size evaluated by[31,36]

$$r^*=\frac{2\gamma_{\mathrm{n}}V_{\mathrm{m}}}{RT}\left[\ln\left(\frac{\bar{c}}{c_{\mathrm{e}}}\right)\right]^{-1} \tag{4}$$

where V_{m} is the molar volume of the precipitates, $\bar{c}$ is the mean solute concentration in the matrix. In the KW type modelling approach, the nucleated precipitates can only grow if their size is greater than the critical size and generally the precipitate size is set 10% greater than the calculated critical size.[31,36]

The volume of the rod like S phase precipitates is evaluated by including the aspect ratio ($a_{\mathrm{r}}=l/2r$), where l is the length and r is the cross-sectional radius of the precipitates. The value of a_{r} is taken as constant in the present model. The volume of each of the S phase precipitates $V_{\mathrm{S,j}}$ is evaluated by

$$V_{\mathrm{S,j}}=\pi r_{\mathrm{j}}^2 l_{\mathrm{j}}=2\pi r_{\mathrm{j}}^3 a_{\mathrm{r}} \tag{5}$$

where a_{r} is considered to be in good approximation constant, and its value is determined from TEM work on isothermally aged alloys ($a_{\mathrm{r}}=10$).[29]

The growth and coarsening of the S phase precipitates are also assumed to be controlled by the diffusion of the slowest diffusing element (Cu in this case) to the precipitate/matrix interface. During each time step the growth and coarsening of the existing groups of precipitates is evaluated by a single rate equation[37–40]

$$\frac{\mathrm{d}r}{\mathrm{d}t}=\frac{D}{r}\frac{\bar{c}-c_{\mathrm{i}}}{c_\beta-c_{\mathrm{i}}} \tag{6}$$

where c_β is the solute concentration in the precipitate, D is the diffusion coefficient, r is the precipitate radius and c_{i} is the solute concentration at the precipitate/matrix interface that is evaluated by the Gibbs–Thompson relationship.[41–43] The formulation of the Gibbs–Thompson used for determining c_{i} is given by[44]

$$c_{\mathrm{i}}=c_{\mathrm{e}}\exp\left(\frac{2\gamma_{\mathrm{g}}V_{\mathrm{m}}}{c_\beta rRT}\right) \tag{7}$$

(Note that this is different from other models,[25–28] the derivation for the latter equation is provided in Ref. 44.)

In the model, it is assumed that all Cu and Mg not taken up by other precipitates will form co-clusters up to an amount determined by the semiequilibrium solvus for the co-clusters. The volume fraction of the Cu–Mg co-clusters transformed is evaluated by

$$f^{\mathrm{cl}}=\frac{(\bar{c}-c_{\mathrm{e}}^{\mathrm{cl}})}{c_\beta^{\mathrm{cl}}} \tag{8}$$

where c_β^{cl} is the solute concentration in the Cu–Mg co-clusters.

Strength model

The strength model includes strengthening contributions from the Cu–Mg co-clusters, S phase, dislocations introduced by stretching during T351 treatment and the solid solution. The co-clusters are relatively weak obstacles that can be sheared by dislocations. It has been shown that the critical resolved shear stress (CRSS) of the grains due to the co-clusters can be described well by the modulus strengthening mechanism, the magnitude of which can be represented as[16,17,45,46]

$$\Delta\tau_{cl} = \frac{\Delta\mu}{4\pi(2)^{1/2}}\left(f^{cl}\right)^{1/2} \tag{9}$$

where f^{cl} is the volume fraction of the clusters and $\Delta\mu$ is the difference in the shear modulus of the matrix and the clusters, which was obtained by comparison with strength data during isothermal ageing,[29] providing $\Delta\mu$=4·03 GPa. This procedure was justified through comparison of strength evolution, cluster composition (as assessed through atom probe field ion microscopy) and amount of co-clusters (as assessed by calorimetry) in alloys that contained only co-clusters.[17]

S phase precipitates are approximately rod shaped aligned in the {100} directions.[15,47] Their cross-section on slip planes (i.e. the area of precipitate cut through by the slip plane) is generally larger than several nanometres, and these precipitates are mostly considered to be non-shearable for the purpose of determining the yield strength. Through computer simulation of equilibrium configurations of a dislocation interacting with randomly distributed non-shearable circular obstacles of finite size in a slip plane, Zhu and Starke[48] identified the following modification of the Orowan equation

$$\Delta\tau_S = \frac{0{\cdot}82\mu_{Al}b}{2\pi L_{cc}}\ln\left(\frac{d}{r_o}\right)\left[1+0{\cdot}83\frac{d}{L_{cc}}+1{\cdot}91\left(\frac{d}{L_{cc}}\right)^2\right] \tag{10}$$

where d is the diameter of the obstacle, L_{cc} is the planar (centre to centre) spacing between the obstacles in the slip plane, b is the magnitude of the Burgers vector and r_o is the inner cutoff radius for calculation of the dislocation line tension, which is generally considered equal to b. In the case of rod like precipitates oriented along {100} for which length of the precipitates L_r is much larger than the diameter D_r, it holds

$$D = \frac{D_r}{[\cos(54{\cdot}7^\circ)]^{1/2}} \tag{11}$$

$$L_{cc} = D_r\left[\frac{\pi}{4f\cos(54{\cdot}7^\circ)}\right]^{1/2} \tag{12}$$

where f is the volume fraction of the rod shaped precipitates.

Using the latter two expressions for D and L_{cc}, equation (10) may be written as

$$\Delta\tau_S = \frac{0.112\mu_{Al}b}{D_r}\ln\left(\frac{1.316D_r}{r_o}\right)\left(f^{1/2}+0.94f+2.44f^{3/2}\right) \tag{13a}$$

(Note that while the derivation is similar, the coefficients 0·94 and 2·44 are different to the ones given in the corresponding equation elsewhere.[48] In practice this will make little difference for predictions as $f \ll 1$. The authors believe equation (13a) is the correct derivation.)

The latter equation is considered to be the most advanced and accurate treatment of strengthening due to non-shearable rod shaped precipitates of uniform size in a matrix of uniform resistance to dislocation movement. However, in most real alloys some deviations from this ideal case can be expected because:

(i) precipitates are not quite perfect cylinders
(ii) precipitates will have a range of sizes
(iii) dislocation movement in the matrix near the precipitates is likely to be hampered by the strain field near precipitates.

These deviations from the ideal case will all tend to increase the strengthening related to the precipitates with respect to the latter equation. Thus a calibrating factor will be added to the latter equation. From isothermal precipitation hardening data, this factor was determined to be 1·4,[29] e.g.

$$\Delta\tau_S = 1.4\frac{0.112\mu_{Al}b}{D_r}\ln\left(\frac{1.316D_r}{r_o}\right)\left(f^{1/2}+0.94f+2.44f^{3/2}\right) \tag{13b}$$

The total CRSS of the grains $\Delta\tau_{tot}$ is evaluated using the phenomenological Pythagorean and linear superposition approximations, which are used for summation of the obstacle strengths of similar and different magnitudes respectively[49–51]

$$\Delta\tau_{tot} = \Delta\tau_{ss} + \left(\Delta\tau_S^2+\Delta\tau_{cl}^2+\Delta\tau_d^2\right)^{1/2} \tag{14}$$

where $\Delta\tau_{ss}$ and $\Delta\tau_d$ are the increase in CRSS of the grains due to the solute in the matrix and the dislocations[52] respectively.

To compare with the macroscopic deformation data the total CRSS of the grains is converted to yield strength by considering that for the present alloys elastic and plastic anisotropy of grains is limited and that hence a model assuming individual grains deform as if embedded in an isotropic medium is appropriate. In such a case, yield strength σ_y can be approximated accurately as a linear function of the CRSS

$$\sigma_y = \sigma_{GB} + M\Delta\tau_{ss} \tag{15}$$

where σ_{GB} is a grain boundary strengthening contribution and proportionality factor M is taken as 2·6 for Al alloys.[51] For the present alloys σ_{GB} has little impact on the predictions as it is relatively small.[53]

For Al–Cu–Mg alloys the hardness for aged conditions is not proportional to proof strength,[54] and hence a non-linear conversion is used. Proportionality is only observed when strengthening is either dominated by clusters (i.e. in substantially underaged conditions) or dominated by S phase (i.e. in peak aged and overaged conditions). Hence yield strength data will be converted into hardness using a weighted average of two proportionality constants λ_1 and λ_2 weighted by the contributions of co-clusters and S phase to the critical resolved shear stress of the grains

$$\sigma_y = \frac{\lambda_1\Delta\tau_{cl}+\lambda_2\Delta\tau_S}{\Delta\tau_{cl}+\Delta\tau_S}HV \tag{16}$$

where $\Delta\tau_{cl}$ is the predicted contribution of co-clusters to

the critical resolved shear stress of the grains and $\Delta\tau_S$ is the predicted contribution of S phase to the critical resolved shear stress of the grains. λ_1 and λ_2 were chosen such that they represent previously published data,[54] yielding $\lambda_1=2{\cdot}2$ and $\lambda_2=3{\cdot}2$. Although this non-linear conversion is quite sophisticated and has been shown to be valid over a wide range of heat treatments, it should be taken into account that some minor inaccuracies (typically $\sim$10 MPa) in determination of yield strength may be encountered.

Experimental

The model predictions are verified by the hardness and calorimetry data measured on a 2024-T351 Al–Cu–Mg alloy supplied as 12·5 mm thick plate. The alloy composition is Al–4·2Cu–1·36Mg–0·58Mn–0·06Si–0·08Fe (wt-%). The material was solution treated, stretched (2%) and aged at room temperature for several months to obtain a stable state. Electron backscatter diffraction on a scanning electron microscope identified the grain structure of the alloys to be recrystallised, with weak crystallographic texture.

For DSC experiments and non-isothermal heat treatments, samples ($\sim5\times5\times2$ mm) were cut using a precision saw, the corners were ground and the surfaces were polished up to 1200 grit. Two different non-isothermal treatments were carried out on the samples at heating rates of 10 and 50°C min^{-1} which were followed by cooling at 50°C min^{-1} to room temperature in a Perkin Elmer Pyris-1 power compensation type DSC instrument.

Differential scanning calorimetry scans were made over the temperature range from 50 to 500°C for heating rates of 10 and 50°C min^{-1}. The DSC curves presented in the present work show the heat flows after correction for baseline and heat capacity effects,[55] i.e. they represent the heat flow due to reactions in the sample.

Vickers microhardness was carried out on samples heat treated non-isothermally in the DSC equipment. The heat treatment cycle consisted of a ramp at 10 or 50°C min^{-1} to 13 different temperatures (100, 150, 200, 240, 260, 280, 290, 300, 340, 400, 450 and 500°C) followed by cooling to room temperature at 50°C min^{-1}. All hardness tests were carried out at room temperature immediately after cooling the heat treated samples to room temperature. On each sample three indentations were carried out with a load of 1 kgf and the average value of the hardness is reported.

2024-T351 samples heat treated at 10°C min^{-1} up to 300 and 420°C, followed by cooling at 50°C min^{-1} to room temperature were investigated in a Jeol JEM 3010 transmission electron microscope. These two treatments were selected because they represent critical and distinct stages in the precipitate evolution just before coarsening and in an advanced stage of coarsening. The TEM samples were prepared by cutting a thin slice ($\sim$0·3 mm), grinding it to a thickness of $\sim$0·15 mm and punching 3 mm diameter discs. The samples were polished in a twin jet electro polisher using a 30%HNO_3 solution in methanol maintained between −20 and −30°C. Digital bright field images taken near the [001] zone axis were analysed manually using the dimension feature in AutoCAD software to manually measure the S phase precipitate size.

Results and model evaluation

The key parameter in the model is the precipitate/matrix interfacial energy. Following other works,[23,56] the interfacial energy is considered as temperature dependant and to undergo an increase during transition from the nucleation to coarsening stages during ageing. In previous work[29] it was shown that the temperature dependence could be treated well by a single T^3 term in the expressions for interfacial energy, and thus the two equations for the evaluation of the interfacial energy adopted here are

$$\gamma_g=\gamma_{n,0}-aT^3 \quad \text{[within nucleation /growth regime (when the nucleation rate} > 0)] \tag{17}$$

$$\gamma_g=\gamma_n+\Delta\gamma \quad \text{[within coarsening regime (when the nucleation rate} = 0)] \tag{18}$$

where γ_n is the interfacial energy during nucleation (units J m^{-2}), T is the absolute temperature, γ_g is the interfacial energy during growth (units J m^{-2}) and $\Delta\gamma$, $\gamma_{n,0}$ and a are fitting parameters. The values of the fitting parameters have been obtained using a trial and error procedure to fit both the measured resulting hardness and heat flow data for the non-isothermal treatments reported in the present work. As expected, reasonably good fits were obtained with $\Delta\gamma$ and a identical to the ones determined in the modelling of isothermal precipitation hardening data presented previously.[29] However a slight increase in the value of $\gamma_{n,0}$, from 0·1206 J m^{-2},[29] obtained through fitting the model to isothermal ageing data, to 0·1238 J m^{-2} for the present model by fitting to controlled heating and cooling data, proved necessary to obtain good fits. Especially peak hardness is very sensitive to $\gamma_{n,0}$ as the density of precipitates at peak aged condition varies strongly with variations in this interfacial energy. The issues related to interfacial energy are discussed in the companion paper.

The model predictions of the change in hardness during non-isothermal heating at 10 and 50°C min^{-1} are compared with the experimentally measured hardness values in Fig. 1. (Note these predictions are for the room temperature hardness, i.e. the hardness for the case that the heat treatment would be interrupted by a very fast quench to room temperature, with no microstructural changes occurring during the quench.) The data points represent the hardness values measured after heating the samples at 10 and 50°C min^{-1} up to a peak temperature and cooling to room temperature at 50°C min^{-1} in the DSC. The dotted line denotes the predicted hardness considering no S phase nucleates during the cooling. These predictions during heating are generally in good agreement up to 350°C but are significantly higher than the measured values at higher temperatures. To more accurately model the changes for the higher temperature treatments, the S phase formation during the cooling cycle was included (solid line in Fig. 1). In this expansion of the model, the interfacial energy during the cooling cycle, for cases where S phase remains present during the whole of the cycle is the same as during the coarsening stage of the heating cycle. However, when S phase is dissolved (for treatments

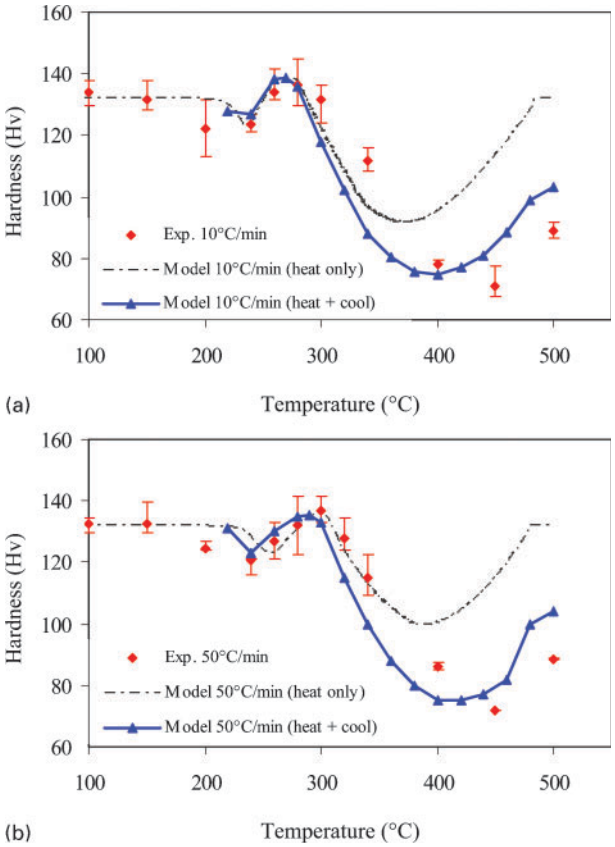

1 Model predictions of hardness of samples during non-isothermal heating at *a* 10 and *b* 50°C min^{-1} are compared with experimental results of hardness measured after heating at 10 and 50°C min^{-1} followed by cooling at 50°C min^{-1}

with maximum temperature exceeding ~475°C), and thus needs to renucleate during cooling, the treatment for the nucleation/growth regime given by equation (17) is used. The predictions are in good agreement with the experimentally measured hardness values for the entire temperature range. From these results the effect of microstructural changes during cooling on the hardness values is evident. Figure 2 shows the predicted changes in the hardness and evolution of the S phase average size and volume fraction during the heating and cooling cycles. It is observed that during the cooling cycle there is no apparent change in the predicted average precipitate size up to the temperature for peak hardness (280°C for 10°C min^{-1} and 300°C for 50°C min^{-1}) but at higher temperatures it increases, and it is the main cause for the decrease in the predicted hardness. This explains the difference in the predicted hardness results for the heating only and the heating and cooling cycles in Fig. 1.

The model is also verified by comparing the heat flow due to the formation and dissolution of the S phase with the DSC scans obtained during heating at 10 and 50°C min^{-1} for the temperature range 0 to 500°C, presented in Fig. 3. The heat effects observed in the DSC scans have been identified in previous work through TEM and three-dimensional atom probe studies.[15,16,17,19,54,55,57] The main exothermic effect (appearing between 250 and 350°C, depending on heating rate and previous heat treatment) is due to the S phase formation. The endothermic effect occurring before the S phase formation effect is mainly due to the co-cluster dissolution and the endothermic effect occurring after the S phase formation effect up to 490°C is due to the S phase dissolution.[54,55] In the modelled heat flow, the relatively sharp endothermic peak at start of the broader endothermic S phase dissolution effect is a direct result of the change in interfacial energy of the precipitates imposed in the model at the completion of nucleation, which causes some of the smaller precipitates to dissolve. This should be considered a transitory artefact introduced by this particular aspect of the KW model, and it could be resolved, be it in a rather arbitrary way, by allowing the changes in interfacial energy to occur more gradually. Ignoring this transitory artefact in Fig. 3, there is a very good agreement between the measured and the predicted heat flows representing the formation and dissolution of the S phase (co-cluster dissolution was not included in the predicted curve), with a slight shift of ~5°C. A relatively better agreement simultaneously in the strength and heat flow prediction and experimental results may be obtained by slightly adjusting the values of the factor in equation (13b) and $\gamma_{n,0}$ in equation (17). However, in the present model the value of the factor in equation (13b) is kept the same (i.e. 1·4) as in the previously developed and tested isothermal model.[29] The modelled heat flow should be proportional to the rate of change of total amount of S phase, dV_S/dt, and the regular solution model predicts it should equal $\Delta H_S \times dV_S/dt$. Indeed, peak heat flows correspond closely to this prediction. The authors have added normalising factors, all close to unity, such that peak heat flows coincide.

Another test of the model is performed by comparing the predicted average precipitate size with size measured from TEM graphs obtained after heating the samples at 10°C min^{-1} up to 300 and 420°C followed by cooling at 50°C min^{-1} to room temperature, presented in Fig. 4. The predicted values are in good agreement with the measured values. The measured data are listed in Table 1. (Standard error in the mean is calculated by dividing the standard deviation by the square root of the number of precipitates measured.) It should be noted here that the general shape of the average size *v.* temperature and average size *v.* time evolutions of precipitates in alloys are generally accepted to conform to a general pattern of initial accelerating growth, deceleration due to impingement, near constant size during a transition period, finally followed by coarsening which is well represented by the general Lifshitz–Slyozov–Wagner coarsening expression. The authors' model predictions are consistent with this. The authors have here elected to test their model through investigation of the microstructure by direct imaging using TEM for two critical and distinct stages, and it is thought that further TEM experiments would not add substantially to the critical testing of the size evolution of S phase predicted by the model. (However, microstructural investigation after heat treatments that favour formation of metastable phases or ones that favour the formation Ω phase may provide data for further refinement of models.)

In the model it has been assumed that cluster reformation during room temperature ageing results in a significant increase in the hardness. To analyse this additional DSC and hardness experiments were

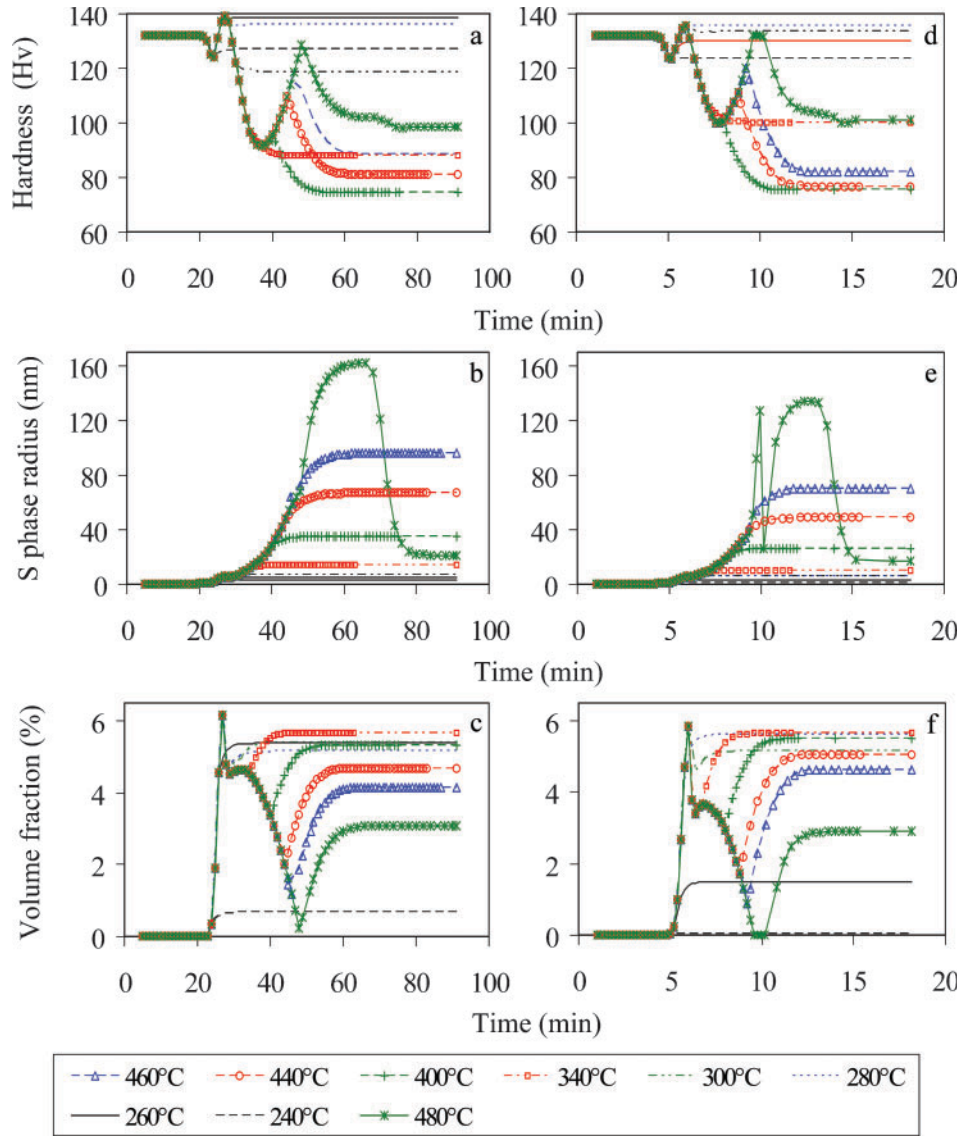

2 Model predictions of hardness, S phase average size and volume fraction as function of ageing time during non-isothermal heating at *a–c* 10 and *d–f* 50°C min^{-1} to peak temperature and followed by cooling to room temperature at 50°C min^{-1}

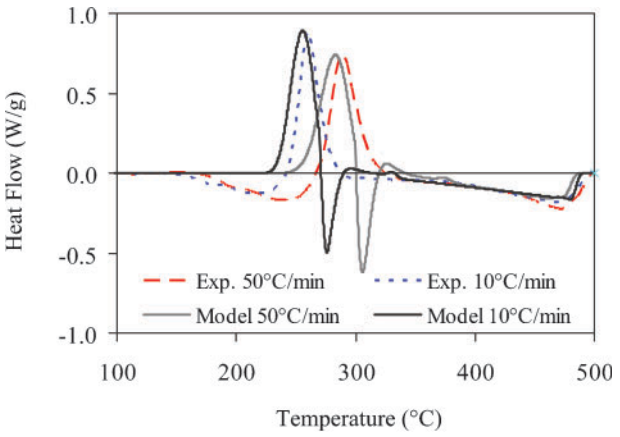

3 Model predictions of heat flow due to S phase formation and dissolution during heating at 10 and 50°C min^{-1} are compared with DSC scans measured for heating rates of 10 and 50°C min^{-1} for temperature range from 0 to 500°C

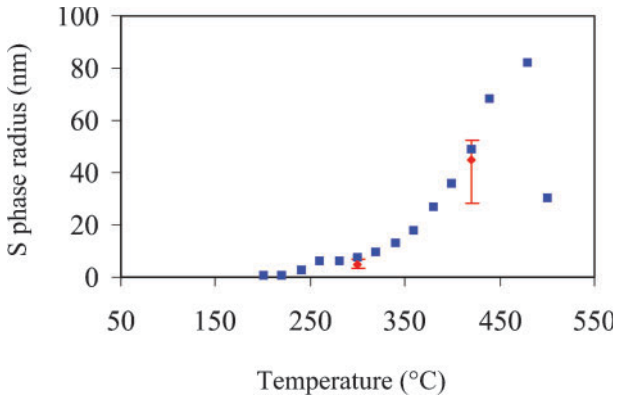

4 Model predictions of S phase radius during heating at 10°C min^{-1} are compared with average radius measured from TEM graphs after heating sample at 10°C min^{-1} up to 300 and 420°C followed by cooling at 50°C min^{-1}

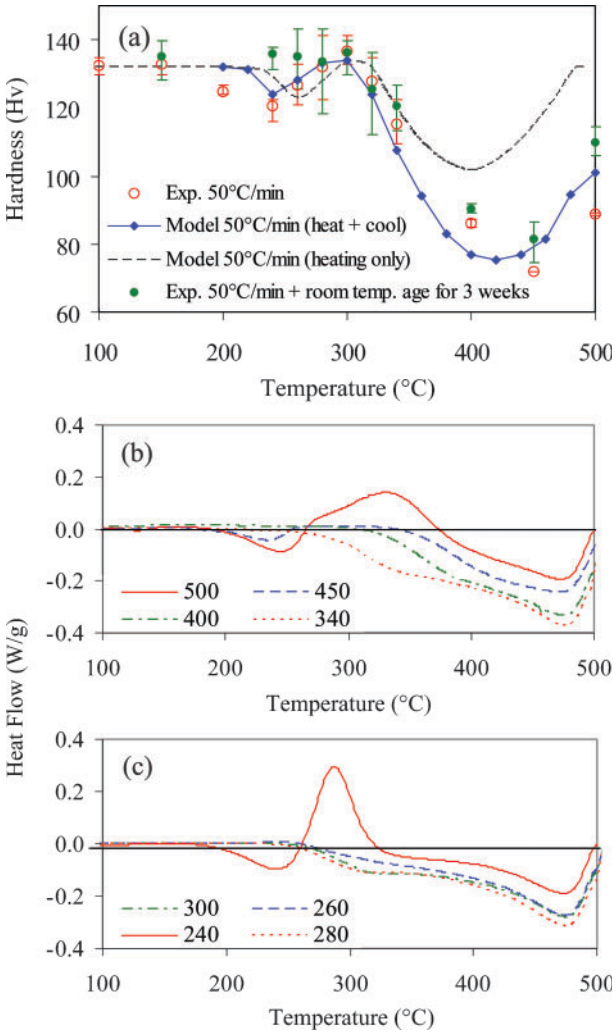

5 ***a*** **hardness measured after heating at 50°C up to peak temperature and cooling at 50°C min^{-1}, compared with that measured on same samples after ageing for 3 weeks at room temperature, and** ***b***, ***c*** **DSC scans measured after 3 weeks ageing at room temperature following heating at 50°C and cooling at 50°C min^{-1} to temperatures indicated**

performed on the samples after ageing at room temperature for 3 weeks, which are presented in Fig. 5. In Fig. 5*a*, a significant increase in the hardness is observed after 3 weeks ageing at room temperature in samples previously heat treated non-isothermally up to 240, 450 and 500°C. In Fig. 5*b* and *c* the DSC scans show a significant endothermic effect due to cluster dissolution (at about 200–260°C) in these samples indicating that co-cluster reformation proceeds during ageing at room temperature. One interesting observation in these experiments is that the co-cluster reformation does not occur in the samples heat treated between 260 and 400°C, when substantial S phase precipitates are present in the alloy, even though at the higher part of this range there is sufficient solute available to form co-clusters following the regular solution model.

Discussion

Modelling of precipitation kinetics in various aluminium alloys based on the KW type approach has been presented in a range of papers[24–26,28,30,31] and in some works the strength predictions have also been made.[36] In the previous works, however, the model assessment is limited to comparison with only the strength data and/or precipitate size data over a limited temperature range (mostly less than 100°C). The present work is the first time a two precipitate ageing model valid over a 500°C range is presented and tested against measurements of the heat flow, the heat flow during heat treatment over a range covering 500°C, and the precipitate size and hardness following these treatments. The model accuracy is mostly very good considering that:

(i) the non-isothermal calorimetry data are fitted well over the entire range from 50 to 500°C
(ii) the hardness data are fitted well over the entire range (heat treatments from 50 to 500°C
(iii) the precipitate sizes are predicted well
(iv) in a previous work,[29] the model predictions also fit well to the isothermal calorimetry and strength data.

The parameters fitted in the model have values that are reasonable, when compared to those reported in the literature for similar works.

A further useful test of model predictions is obtained by comparing the (apparent) activation energies determined from DSC data using isoconversion methods valid for linear heating.[58,59] The activation energy thus derived from the DSC experiments (the data in Fig. 2, plus additional experiments performed at 5, 10, 20 and 25°C min^{-1}) is 132 ± 5 kJ mol^{-1}. This corresponds closely with the activation energy obtained from predicted DSC curves at 10 and 50°C min^{-1} using the same isoconversion methods, which equals 137 kJ mol^{-1}. The close correspondence provides a further indication that the aspects of the model related to thermal activation of the processes are correct. (These values are close to the value of the activation energy for growth of S phase adopted in the model, $E_a^S = 135$ kJ mol^{-1}. This can be taken to support the assumption, made in a range of publications,[55] that activation energy obtained with isoconversion methods derived on the basis of a simplified kinetic model with a single temperature dependent Arrhenius term, equals the activation energy for growth.)

A key point to improve the model is the need to better understand the factors influencing the interfacial energy. While the issue of the two different interfacial energies (one for nucleation and larger one for coarsening) has been discussed,[23,56] and can be rationalised in a

Table 1 Measured average diameter of S precipitates as obtained from TEM

Temperature, °C	Average radius, nm	Standard deviation, nm	Standard error*, nm	No. of measured precipitates
300	4·25	0·90	0·21	17
420	45·0	8·15	1·30	41

*Standard error=standard deviation/$(N)^{1/2}$, where N is the number of measured precipitates.

qualitative sense, current practice still requires these to be fitted based on extensive data, with no possibility of previous prediction. These issues relating to the interfacial energy are further discussed in the companion paper.

Conclusions

A previously developed numerical model based on the KW model for prediction of strengthening during isothermal treatments has been extended to include non-isothermal treatments which consist of controlled heating and cooling. The model includes strengthening contributions due to shearable Cu–Mg co-clusters, the non-shearable S phase precipitates, the solute in the matrix and the dislocations. The model relies on the selection and treatment of the interfacial energy during nucleation, growth and coarsening stages. The model predictions for hardness, heat flow for the formation/dissolution of the S phase and size of the S phase have been compared with the experimentally measured data on 2024 Al–Cu–Mg alloys. The model accuracy is mostly very good considering the following.

1. The non-isothermal calorimetry data are fitted well over the entire range from 50 to 500°C.
2. The hardness data are fitted well over the entire range from 50 to 500°C.
3. The precipitate sizes are predicted well.
4. The model predictions also fit well to the isothermal calorimetry and strength data as was assessed in previous work.

References

1. S. Di, X. Yang, G. Luan and B. Jian: *Mater. Sci. Eng. A*, 2006, **A435–436**, 389.
2. C. Genevois, D. Fabregue, A. Deschamps and W. J. Poole: *Mater. Sci. Eng. A*, 2006, **A441**, 39.
3. D. Mitlin, V. Radmilovic, T. Panc, J. Chena, Z. Feng and M. L. Santella: *Mater. Sci. Eng. A*, 2006, **A441**, 79.
4. S. Lathabai, M. J. Painter, G. M. D. Cantin and V. K. Tyagi: *Scr. Mater.*, 2006, **55**, 899–902.
5. N. Kamp, N. Gao, M. J. Starink and I. Sinclair: *Int. J. Fatigue*, 2007, **29**, 869.
6. H. Kaçar, E. Atik and C. Meriç: *J. Mater. Process. Technol.*, 2003, **142**, 762.
7. G. Liu, G. J. Zhang, X. D. Ding, J. Sun and K. H. Chen: *Mater. Sci. Eng. A*, 2003, **A344**, 113–124.
8. S. P. Ringer, K. Hono, I. J. Polmear and T. Sakurai: *Appl. Surf. Sci.*, 1996, **94–95**, 253.
9. P. Ratchev, B. Verlinden, P. de Smet and P. van Houtte: *Acta Mater.*, 1998, **46**, 3523.
10. S. C. Wang and M. J. Starink: *Int. Mater. Rev.*, 2005, **50**, 193.
11. P. I. Gouma, D. J. Lloyd and M. J. Mills: *Mater. Sci. Eng. A*, 2001, **A319–321**, 438.
12. A. M. Zahra and C. Y. Zahra: *Scr. Mater.*, 1998, **39**, 1558.
13. Y. A. Bagaryatsky: *Dokl Akad SSSR*, 1952, **87**, 559.
14. L. Kovarik, M. K. Miller, S. A. Court and M. J. Mills: *Acta Mater.*, 2006, **54**, 1731.
15. S. C. Wang and M. J. Starink: *Acta Mater.*, 2007, **55**, 933.
16. S. C. Wang, M. J. Starink and N. Gao: *Scr. Mater.*, 2006, **54**, 287.
17. M. J. Starink, N. Gao, L. Davin, J. Yan and A. Cerezo: *Phil. Mag.*, 2005, **85**, 1395,
18. M. J. Starink, A. Cerezo, J. Yan and N. Gao: *Phil. Mag. Lett.*, 2006, **86**, 243.
19. N. Gao, L. Davin, S. Wang, A. Cerezo and M. J. Starink: *Mater. Sci. Forum*, 2002, 396–**402**, 923.
20. Y. Nagai, M. Murayama, Z. Tang, T. Nonaka, K. Hono and M. Hasegawa: *Acta Mater.*, 2001, **49**, 913.
21. R. Wagner and R. Kampmann: *Mater. Sci. Technol. A*, 1991, **5A**, 213.
22. A. Deschamps and Y. Brechet: *Acta Mater.*, 1999, **47**, 293.
23. J. C. Werenskiold, A. Deschamps and Y. Brechet: *Mater. Sci. Eng. A*, 2000, **A293**, 267–274.
24. O. R. Myhr, Ø. Grong and S. J. Andersen: *Acta Mater.*, 2001, **49**, 65–75.
25. J. D. Robson: *Acta Mater.*, 2004, **52**, 1409–1421.
26. M. Nicolas and A. Deschamps: *Acta Mater.*, 2003, **51**, 6077–6094.
27. C. Genevois, A. Deschamps, A. Denquin and B. Doisneau-Cottignies: *Acta Mater.*, 2005, **53**, 2447–2458.
28. N. Kamp, A. Sullivan, R. Tomasi and J. D. Robson: *Acta Mater.*, 2006, **54**, 2003.
29. I. N. Khan, M. J. Starink and J. L. Yan: *Mater. Sci. Eng. A*, 2008, **A472**, 66–74.
30. J. D. Robson and P. B. Prangnell: *Acta Mater.*, 2001, **49**, 599.
31. J. D. Robson: *Mater. Sci. Eng. A*, 2002, **A338**, 219.
32. O. R. Myhr and Ø. Grong: *Acta Mater.*, 2000, **48**, 1605.
33. M. J. Starink and J. Yan: Proc. 1st Int. Symp. on 'Metallurgical modelling for aluminium alloys', Pittsburgh, PA, USA, October 2003, ASM International, 119.
34. J. W. Christian: 'Theory of transformations in metals and alloys', Part 1; 1975, Oxford, Pergamon Press.
35. M. J. Stowell: *Mater. Sci. Technol.*, 2002, **18**, 139.
36. O. R. Myhr, Ø. Grong, H. G. Fjaer and C. D. Marioara: *Acta Mater.*, 2004, **52**, 4997.
37. C. Zener: *J. Appl. Phys.*, 1949, **20**, 950.
38. H. B. Aaron, D. Fainstain and G. R. Kotler: *J. Appl. Phys.*, 1970, **41**, 4404.
39. J. S. Langer and A. J. Schwartz: *Phys. Rev. A*, 1980, **21A**, 948.
40. G. Madras and B. J. McCoy: *Chem. Eng. Sci.*, 2004, **59**, 2753.
41. O. R. Myhr, Ø. Grong and A. J. Anderson: *Acta Mater.*, 2001, **49**, 65–75.
42. G. Madras and B. McCoy: *Acta Mater.*, 2003, **51**, 2031–2040.
43. T. Miyazaki, T. Koyama and S. Kobayashi: *Metall. Trans. A*, 1996, **27A**, 945–949.
44. M. Perez: *Scr. Mater.*, 2005, **52**, 709.
45. L. Cartaud, J. Guillot and J. Grilhe: Proc. 4th Int. Conf. on 'The strength of metals and alloys', ICSMA 4, Nancy, France, August–September 1976, ASM, Vol. 1, 214.
46. P. Gomiero, Y. Brechet, F. Louchet, A. Tourabi and B. Wack: *Acta Mater.*, 1992, **40**, 857.
47. S. C. Wang, F. Lefebvre, J. L. Yan, I. Sinclair and M. J. Starink: *Mater. Sci. Eng. A*, 2006, **A431**, 123.
48. A. W. Zhu and E. A. Starke: *Acta Mater.*, 1999, **47**, 3263.
49. M. J. Starink, A. Descamps and S. C. Wang: *Scr. Mater.*, 2008, **58**, 377–382.
50. E. Nembach: *Acta Mater.*, 1992, **40**, 3325.
51. M. J. Starink and S. C. Wang: *Acta Mater.*, 2003, **51**, 5131.
52. M. J. Starink, P. Wang, I. Sinclair and P. J. Gregson: *Acta Mater.*, 1999, **47**, 3855.
53. B. Clausen, T. Lorentzen and T. Leffers: *Acta Mater.*, 1998, **46**, 3087.
54. M. J. Starink, I. Sinclair, N. Gao, N. Kamp, P. J. Gregson, P. D. Pitcher, A. Levers and S. Gardiner: *Mater. Sci. Forum*, 2002, **396–402**, 601.
55. M. J. Starink: *Int. Mater. Rev.*, 2004, **49**, 1916.
56. J. D. Robson, M. J. Jones and P. B. Prangnell: *Acta Mater.*, 2003, **51**, 1453.
57. D. P. P. Booth, M. J. Starink and I. Sinclair: *Mater. Sci. Technol.*, 2007, **23**, 276.
58. M. J. Starink: *Thermochim. Acta*, 2003, **404**, 163.
59. M. J. Starink: *J. Mater. Sci.*, 2007, **42**, 483.